# Solution-processable ultrathin size- and shape-controlled colloidal $Cu_{2-x}S$ nanosheets

*Chemistry of Materials* **2015, *27*, 283-291. DOI: 10.1021/cm503929q**

# Solution-Processable Ultrathin Size- and Shape-Controlled Colloidal $Cu_{2-x}S$ Nanosheets

*Ward van der Stam[1], Quinten A. Akkerman[1], Xiaoxing Ke[2], Marijn A. van Huis[3], Sara Bals[2] and Celso de Mello Donega[1]**

[1]Condensed Matter and Interfaces, Debye Institute for Nanomaterials Science, Utrecht University, Princetonplein 5, 3584 CC Utrecht, The Netherlands

[2]Electron Microscopy for Materials Science (EMAT), University of Antwerp, Groenenborgerlaan 171, B-2020 Antwerp, Belgium

[3]Soft Condensed Matter, Debye Institute for Nanomaterials Science, Utrecht University, Princetonplein 5, 3584 CC Utrecht, The Netherlands

***Corresponding Author:** c.demello-donega@uu.nl

**ABSTRACT**. Ultrathin 2-dimensional (2D) nanosheets (NSs) possess extraordinary properties that are attractive for both fundamental studies and technological devices. Solution-based "bottom-up" methods are emerging as promising routes to produce free-standing NSs, but the synthesis of colloidal NSs with well-defined size and shape has remained a major challenge. In this work we report a novel method that yields 2 nm thick colloidal $Cu_{2-x}S$ NSs with well-defined shape (triangular or hexagonal) and size (100 nm to 3 μm). The key feature of our approach is the use of a synergistic interaction between halides (Br or Cl) and copper-thiolate metal-organic frameworks to create a template that imposes 2D constraints on the Cu-catalysed C-S thermolysis, resulting in nucleation and growth of colloidal 2D $Cu_{2-x}S$ NSs. Moreover, the NS composition can be post-synthetically tailored by exploiting topotactic cation exchange reactions. This is illustrated by converting the $Cu_{2-x}S$ NSs into ZnS and CdS NSs while preserving their size and shape. The method presented here thus holds great promise as a route to solution-processable compositionally diverse ultrathin colloidal NSs with well-defined shape and size.

**KEYWORDS:** ultrathin two-dimensional materials, colloidal nanosheets, metal-organic frameworks, copper sulfide, 2D growth

## Introduction

Ultrathin 2-dimensional (2D) nanomaterials (nanosheets, NSs) are attracting increasing research efforts due to their extraordinary electronic, phononic, optical and mechanical properties.[1-9] Well-known examples are graphene and transition-metal dichalcogenides (*e.g.*, $MoS_2$).[1-9] An essential feature of ultrathin NSs is that they are just a few atomic monolayers thick ($w \leq$ 2.5 nm), but have lateral dimensions ($L$) of at least 100 nm. This creates a strong 1D quantum confinement, which results in unique properties.[1-9] NSs offer compelling opportunities for fundamental studies in 2D physics and hold an immense potential for spintronic devices, field-effect transistors, nanoscale sensors, and as building blocks for batteries, photodetectors, and LEDs.[1-9] NSs are typically obtained by exfoliation of bulk materials or grown on substrates by MBE or CVD.[1-9] These methods are however not suitable to produce large amounts of free-standing NSs and lack control over their shape and lateral dimensions.

Solution-based "bottom-up" colloidal chemical methods offer an appealing alternative, and are emerging as promising routes to free-standing colloidal inorganic NSs, due to their versatility in terms of composition, size, shape and surface control. Nevertheless, ultrathin colloidal NSs of inorganic semiconductors are still restricted to just a few materials.[10-27] The most investigated ones are CdX (X= S, Se, Te) nanoplatelets ($w$= 1.2 – 2.1 nm; $L$= 10-700 nm, square or rectangular with irregular edges)[10-13] and nanoribbons ($L \leq$ 1 μm, tens of nm wide),[14-17] which have been shown to possess remarkable optical properties.[10,14,16,18-20] Ultrathin colloidal NSs of $Sb_2S_3$ ($w$= 1.8 nm; rectangular with ragged edges, $L$= 100 x 500 nm),[21] SnSe ($w$= 1 nm, $L$= 300 nm, irregularly shaped),[22] PbS ($w$= 2.8 nm, square, $L \leq$ 1 μm),[23,24] ZnSe ($w$= 1.4 nm, $L$= 40-160 nm, rectangular ribbons ~20 nm wide),[25] β–$In_2S_3$ ($w$= 0.76 nm, $L$= 22-60 nm, hexagonal),[26] and

$Cu_{1.96}S$ (*w*= 0.65 nm, mixed triangular and hexagonal, *L*= 200 nm)[27] have also been recently synthesized. Despite these recent advances, full control over the shape and dimensions of the NSs remains a challenge. Here we demonstrate a synthesis method that yields free-standing ultrathin (2 nm) $Cu_{2-x}S$ NSs with well-defined shape (triangular or hexagonal) and sizes tunable from 100 nm to 3 μm. Moreover, these NSs do not easily fold or entangle themselves, and readily self-assemble into ordered stacks. The key feature of our approach is the use of a synergistic interaction between halides (Br or Cl) and copper-thiolate metal-organic frameworks to create a template that imposes 2D constraints on the Cu-catalysed C-S thermolysis, resulting in nucleation and growth of colloidal $Cu_{2-x}S$ NSs.

$Cu_{2-x}S$ is a direct p-type semiconductor with a band-gap that depends on its stoichiometry (1.1-1.4 eV for x= 0–0.04; 1.5 eV for x= 0.2; 2.0 eV for x= 1).[28] The combination of a suitable band gap, high absorption coefficient, low cost, and low toxicity has made $Cu_{2-x}S$ a prime candidate for the large scale deployment of photovoltaics.[28,29] Moreover, copper chalcogenide nanocrystals (NCs) have been shown to possess the unique property of holding quantum confined excitons and highly tunable localized surface plasmons on demand, opening up the way to create coupled plasmon-excitons in the same NC.[30-32] This creates a number of exciting possibilities, such as ultrafast optical switching or plasmon-enhanced photovoltaics.[30] $Cu_{2-x}S$ NCs also hold promise for biomedical applications[33] and as electrodes for Li-ion batteries.[28] The availability of ultrathin size- and shape-controlled colloidal $Cu_{2-x}S$ NSs may thus prove beneficial for a number of fundamental studies and potential applications. Furthermore, monovalent copper cations have a high solid state mobility due to their small size and low charge, and are therefore easily exchanged by other cations *via* topotactic place exchange reactions, which allow the shape and size of the parent NC to be preserved in the product

NC.[34,35] This has made copper chalcogenide NCs a versatile nanoscale template for the preparation of NCs that cannot be synthesized by direct routes.[34,35] In the present work, we demonstrate the potential of topotactic cation exchange reactions to post-synthetically tailor the composition of the ultrathin colloidal $Cu_{2-x}S$ NSs by converting them into ZnS and CdS, while preserving their well-defined shape, lateral dimensions and thickness.

## Experimental Section

**Materials.** Copper(I) acetate (Cu(OAc), 97%), tin(IV) tetrabromide ($SnBr_4$, 99%), tin(II) dibromide ($SnBr_2$), tin(IV) tetrachloride pentahydrate ($SnCl_4.5H_2O$, 98%), tin(IV) acetate ($Sn(OAc)_4$), copper(I) chloride (CuCl, 97%), copper(I) bromide (CuBr, 98%), copper(I) iodide (CuI, 98%), sodium bromide (NaBr, ≥99%), sodium chloride (NaCl, 99.999%), potassium iodide (KI, 99.99%), cadmium nitrate tetrahydrate ($Cd(NO_3)_2$, 98%), zinc chloride ($ZnCl_2$, reagent grade, ≥98%), tributylphosphine (TBP, 97%), trioctylphosphine (TOP, 90%), 1-dodecanethiol (DDT, ≥98%), 1-octadecene (ODE, tech., 90%), trioctylphosphine oxide (TOPO, 99%), anhydrous toluene, methanol (MeOH) and butanol (BuOH) were purchased from Sigma Aldrich. Sulfur powder was obtained from Strem Chemicals. All chemicals were used without any further purification, except for ODE and TOPO, which were degassed at 120 °C for 2 h prior to synthesis.

**Synthesis of ultrathin $Cu_{2-x}S$ nanosheets.** The method developed here to synthesize $Cu_{2-x}S$ NSs is based on a synthesis protocol reported in the literature,[36] which was modified by adding $SnBr_4$ (or $SnCl_4$) to the reaction mixture. Typically, 27.3 mg (0.22 mmol) Cu(OAc), 32.85 mg (0.075 mmol) $SnBr_4$, and 0.55 g (1.42 mmol) TOPO were dispersed in 12.5 mL ODE. This

mixture was degassed for 30 min at 100 °C, and subsequently heated to 160 °C. At this temperature, 0.5 mL (2.1 mmol) DDT was swiftly injected. The solution was then purged with $N_2$ and further heated to 220 °C. The reaction was maintained at this temperature for 40 min. Aliquots were extracted during the synthesis in order to monitor the evolution of the reaction. The $Cu_{2-x}S$ NSs were precipitated by adding a methanol:butanol mixture and centrifuging at 3000 rpm for 15 min. Afterwards, the NSs were redispersed in toluene. These washing steps were repeated three times.

**Cation Exchange.** The $Cu^+$ for $Cd^{2+}$ or $Zn^{2+}$ cation exchange in $Cu_{2-x}S$ NSs was performed by using a modification of the method described by Son *et al.*[37] The metal salts that were used were $Cd(NO_3)_2$ and $ZnCl_2$, which were chosen due to the relatively weak bond between the cation and anion, ensuring availability of the cations. 0.14 mmol of metal salt was dissolved in 1 mL MeOH in the presence of a small amount of TBP (100 μL). The NSs solution was diluted by adding 2 mL toluene to 1 mL of NSs solution. The $M^{2+}/Cu^+$ molar ratio in the reaction mixture was ~3. This ratio is a lower limit estimate, since it assumes a 100% yield and no purification losses in the synthesis of the $Cu_{2-x}S$ NSs. After addition of the cation-precursor in MeOH, the solution was stirred vigorously for several days at room temperature. The cation exchanged NSs were precipitated by adding 1:1 MeOH:BuOH, isolated by centrifugation at 3000 rpm (10 min), and redispersed in ~2 mL toluene.

**Characterization.** Samples for optical measurements (absorption, PL, PL excitation and PL decay curves) were prepared by directly dissolving the crude reaction mixture in anhydrous toluene under nitrogen and stored in sealed cuvettes. Samples were also analyzed by (Scanning) Transmission Electron Microscopy ((S)TEM), Energy Dispersive X-Ray Spectroscopy (EDS),

Electron Diffraction (ED), and X-Ray diffraction (XRD). Details regarding the characterization of the samples are provided in the Supporting Information, Methods.

## Results and Discussion

**Solution synthesis of ultrathin colloidal $Cu_{2-x}S$ nanosheets with well-defined size and shape.** Figure 1 shows that $SnBr_4$ has a dramatic impact on the morphology and dimensions of colloidal $Cu_{2-x}S$ nanocrystals (NCs) produced by hot-injection of 1-dodecanethiol (DDT) into a solution of cuprous acetate and trioctylphosphine oxide (TOPO) in octadecene (ODE), inducing the formation of ultrathin hexagonal $Cu_{2-x}S$ nanosheets (NSs, 2 nm thick, 110 nm lateral size, Figure 1b,c). In the absence of $SnBr_4$ nearly spherical $Cu_{2-x}S$ NCs (9 nm diameter) are obtained (Figure 1a). Owing to their uniformity in thickness, the NSs readily self-assemble into ordered stacks (Figure 1c) that give rise to a series of low-angle XRD peaks (Figure 1d, and Supporting Information Figure S1), which can be ascribed to successive diffraction orders from a periodic superstructure. The peak separation (*viz*., ~2.49°) corresponds to a periodicity of ~36.7 Å, indicating that the stacks consist of 2 nm thick $Cu_{2-x}S$ nanosheets separated by one DDT monolayer (the length of a fully extended DDT molecule is 17.7 Å, including the thiol headgroup[38]). This is corroborated by HRTEM images, which show ~2.0 nm thick NSs separated by ~1.6 nm (Figure 2b,d). The fact that the inter-NS separation is similar to the length of one DDT molecule implies that the capping monolayers of neighboring NSs fully interpenetrate each other. This is consistent with the results reported by Pileni and co-workers for alkanethiol capped Ag and $Ag_2S$ nanocrystals,[38] where alkyl chains on adjacent nanocrystals were observed to fully interdigitate for chain lengths equal to or longer than $C_{12}$.

The crystallinity of the nanosheets is clearly evident in the XRD pattern (Figure 1d), in the HRTEM images (Figure 2d), and in the electron diffraction (ED) patterns (Figure 2c). The binary Cu-S system has a very rich phase diagram,[39] and therefore $Cu_{2-x}S$ can crystallize in various equilibrium crystal structures (*viz*., monoclinic low-chalcocite $Cu_2S$, djurleite $Cu_{1.96}S$ and roxbyite $Cu_{1.78}S$, hexagonal high-chalcocite $Cu_2S$, digenite $Cu_{1.8}S$, and covellite CuS, orthorhombic djurleite $Cu_{1.96}S$ and anilite $Cu_{1.75}S$).[39-40] These crystal structures are characterized by either hexagonal or cubic close-packing of S atoms, with Cu atoms positioned at the interstices. Transformations involving rearrangement of S atoms from cubic to hexagonal (and *vice-versa*) are extremely slow, leading to a number of metastable phases (*e.g*., low-digenite $Cu_{1.8}S$, tetragonal $Cu_{2-x}S$ with x= 0.03 – 0.15).[39]

The XRD pattern in Figure 1d also shows a peak at higher angles (47°), which corresponds to a lattice spacing of 2.0 Å. This peak may be assigned to the (1 0 20) reflection of the hexagonal digenite crystal structure (see reference XRD pattern in Figure 1d). However, the ED patterns obtained from single, flat lying NSs are not hexagonal, but tetragonal (Figure 2c). Moreover, HRTEM images of stacks of NSs in a side projection (Figure 2d) reveal an interlayer distance of approximately 3.9±0.2 Å. From a comparison of the experimental structural data (XRD, HRTEM, and ED) with the phase diagram of $Cu_{2-x}S$,[39] we infer that the crystal structure of the NSs is likely the metastable tetragonal $Cu_{2-x}S$ phase, with approximate lattice parameters $a=b=$ 4.0 Å, $c=$ 11.0 Å (Figure 2e-f and Supporting Information, Figure S2 and Supporting discussion). Assuming this structure, the spots observed in the ED pattern (Figure 2c) can be assigned to the (100) and (002) lattice spacings, with the *a* and *c* axes lying in the plane of the NS and the *b* axis perpendicular to it. The *a* and *b* axes are equivalent and could be interchanged. The interlayer distance observed in the HRTEM images (Figure 2d) can then be taken to correspond to the 4.0

Å spacing between the buckled Cu atomic layers along the *b*-axis in the tetragonal $Cu_{2-x}S$ crystal structure (Figure 2e-f and Supporting Information, supporting discussion). This analysis indicates that the peak observed in the XRD pattern (Figure 1d) actually corresponds to the (200) reflection of a metastable tetragonal polymorph of digenite. We suggest the tetragonal phase as the most plausible crystal structure as the beam sensitivity of the sample prohibits a profound determination of the crystal structure.

Energy-Dispersive X-ray Spectroscopy (EDS) was used to analyze the sample, confirming that the NSs are made of $Cu_{2-x}S$ (Supporting Information, Figure S3). Intriguingly, the NSs also contain a significant amount of Br, but are devoid of Sn (average Cu: S: Sn: Br elemental ratios are 2.0±0.2: 1.0: 0: 0.30±0.06), even if the nanocrystals are taken directly from the diluted crude reaction mixture and analyzed without any washing. This implies that Sn and Br play very different roles in the formation of ultrathin $Cu_{2-x}S$ NSs, despite their common origin (*i.e.*, $SnBr_4$).

**Unraveling the roles of Br, Sn and DDT.** To clarify the influence of the different components of the reaction system, a series of control experiments was carried out. The results are summarized in Figure 3 and in the Supporting Information (Table S1). As shown above (Figures 1 and 2) and in Figure 3a, ultrathin hexagonal $Cu_{2-x}S$ NSs are obtained if $SnBr_4$ is added to a reaction system that would otherwise yield spherical $Cu_{2-x}S$ NCs. In contrast, if $Sn(acetate)_4$ is used instead of $SnBr_4$, the reaction still yields small spherical NCs (Figure 3b). The use of $SnBr_2$ instead of $SnBr_4$ yields only irregularly shaped and aggregated sheets (Supporting Information, Figure S4).

The impact of $SnBr_4$ is clearly concentration dependent, since co-existing hexagonal NSs and irregularly shaped thin material are obtained if the concentration of $SnBr_4$ is halved (Figure 3c,

Supporting Information Figure S5). Interestingly, the elemental composition of the irregularly shaped thin material significantly differs from that of the hexagonal NSs (Cu:S:Br ratios are 1.41±0.14: 1.0: 0.03±0.01 and 2.0±0.2: 1.0: 0.30±0.06, respectively, Supporting Information Figure S5). If the concentration of $SnBr_4$ is further reduced to a quarter of that originally used, nanosheets are no longer formed, but instead small $Cu_{2-x}S$ nanodisks (aspect ratio ~2) are obtained (Figure 3d), which readily self-assemble into corn cob superlattices (Supporting Information Figure S6). Co-existing hexagonal NSs and irregularly shaped thin material are also obtained in the absence of $SnBr_4$, provided Cu(acetate) is replaced by CuBr (Figure 3e). Remarkably, if CuBr is used in combination with NaBr only well-defined ultrathin hexagonal $Cu_{2-x}S$ NSs are obtained (Figure 3f).

These observations unambiguously demonstrate that Br plays a pivotal role in the formation of $Cu_{2-x}S$ NSs, while Sn(IV) has only the adjuvant role of ensuring that a sufficiently high concentration of Br is readily available in solution. The failure of $SnBr_2$ to yield well-formed NSs (Supporting Information Figure S4) can be attributed to the lower availability of Br, since Br (a soft Lewis base) forms a much stronger bond with Sn(II) (a soft Lewis acid) than with Sn(IV) (a hard Lewis acid). Furthermore, experiments in which dodecanethiol was replaced by other sulfur sources, clearly demonstrate that well-defined $Cu_{2-x}S$ NSs can be formed only when long chain alkanethiols (DDT and octadecanethiol) are used (Supporting Information Figure S7). For example, phenylethanethiol (a bulky and short thiol) yields only irregularly shaped and aggregated thin material, while elemental sulfur leads to small and polydisperse nanocrystals (Supporting Information, Figure S7). In contrast, 1-octadecanethiol (ODT) yields hexagonal NSs similar to those formed using 1-DDT, except for the larger inter-NS separation in the stacks (*viz*., 2 nm, see Supporting Information, inset Figure S7b). The longer inter-NS separation is consistent

with the increase in length of the alkyl chain from 1.77 nm to 2.5 nm from 1-DDT to 1-ODT, which also results in a higher incidence of gauche defects near the terminal methyl end of the alkyl chain.[38] This allows pseudo rotational motion of the chain about the R-S bond axis, leading to interparticle separations that are shorter than the alkyl chain length.[38]

**Size and shape control.** The lateral dimensions of the NSs can be increased up to ~400 nm, while preserving their shape, by diluting the reaction system with ODE (Figure 4a,b, Supporting Information, Figure S8 and Table S1). The lateral dimensions of the hexagonal NSs can also be increased by decreasing the concentration of the coordinating ligand TOPO (Figure 4d), allowing the synthesis of 2 μm wide hexagonal NSs. In contrast, the total absence of TOPO changes both the lateral dimensions and shape of the NSs, yielding large (3-4 μm) triangular NSs (Figure 4c). These experiments clearly demonstrate that TOPO affects the shape of the NSs, converting them from triangular to hexagonal, while simultaneously decreasing the lateral growth rates. The thickness of the nanosheets is not affected, as confirmed by XRD measurements (Figure S9), resulting in well-defined 2 nm-thick hexagonal nanosheets with aspect ratios up to 1000.

The size and shape of the NSs can also be tailored by using $SnCl_4$ instead of $SnBr_4$, although a higher concentration of $SnCl_4$ is required to produce ultrathin NSs (Figure 4e,f). It is noteworthy that the use of $SnCl_4$ instead of $SnBr_4$ changes the NS shape from hexagonal to triangular. The effect is clearly due to the Cl, since a similar result is obtained by replacing Cu(acetate) and $SnCl_4$ by CuCl and NaCl, respectively, in the absence of any other additive (Supporting Information, Figure S10 and Table S1). The fact that a higher concentration of $SnCl_4$ is needed to form NSs can be ascribed to the lower Cl availability due to the stronger Sn-Cl bond.

Interestingly, ultrathin NSs are not obtained if CuCl and NaCl are replaced by CuI and KI, respectively. Instead, this reaction yields a (seemingly) 3D porous network of interconnected particles (Supporting Information, Figure S11). The differences between the effect of different halides (X) can be tentatively ascribed to changes in the Cu-X bond strength. Since Cu(I) is a very soft Lewis acid, the Cu-X bond should become stronger in the sequence Cl<Br<I, as a result of the increase in the soft character of the halides as Lewis bases. This point will be discussed in more detail in the mechanism section below.

**Formation Mechanism.** Several mechanisms have been proposed for the formation of ultrathin colloidal NSs of semiconductors: 2D oriented attachment of PbS NCs,[23] self-assembly of $(CdX)_n$ (X= S, Se) magic-size clusters (MSCs) within 2D lamellar templates,[14-17] 2D growth by monomer addition to $(CdX)_n$ MSC seeds,[10-11] and 2D-constrained growth of CdSe nanodisks within soft-templates formed by close-packed fatty acid layers.[12] It is interesting to note that recent work by Buhro and co-workers has provided compelling evidence that the formation of PbS nanosheets by 2D oriented attachment of small PbS nanoparticles is directed by lamellar-mesophase templates.[24] A soft-template mechanism has also been proposed to explain the formation of slightly thicker ($w$ = 3.2 nm) covellite CuS nanosheets.[41] To investigate whether a soft template mechanism is also involved in the formation of the ultrathin $Cu_{2-x}S$ NSs reported in the present work, we followed the evolution of the reaction by TEM and optical spectroscopy.

Directly after DDT injection, irregularly shaped thin sheets form (Figure 5a). As the reaction progresses, the irregular thin sheets gradually disappear, while hexagonal $Cu_{2-x}S$ NSs form and increase in concentration, eventually becoming the only nanostructure present (Figure 5). The temporal evolution observed in Figure 5 bears similarities with that previously reported for the reaction between Cu(I) salts and DDT in solution at high temperatures (185-220 °C),[36,42] where

irregularly shaped thin sheets are also observed at early reaction times and gradually disappear as $Cu_{2-x}S$ NCs are formed.[36,42] Nevertheless, in these cases ultrathin NSs are not formed, but instead the reaction yields either spherical NCs (5-18 nm)[36,42] or small nanodisks (9 by 13-17 nm),[36] in striking contrast with the present results. This difference is remarkable, and is clearly due to the presence of tin tetrahalides. Tin(IV) compounds (*viz.*, $SnCl_4$ and Sn(acetylacetonate)$_2Cl_2$) have been previously shown to affect the shape of $Cu_{2-x}S$ NCs obtained by reacting Cu(II)acetylacetonate and neat DDT, leading to the formation of either aggregated ultrathin $Cu_{1.96}S$ NSs (*w*= 0.65 nm, *L*= 200 nm, hexagonal or triangular without shape selectivity)[27] or $Cu_{2-x}S$ nanodisks (*w*= 3.2–6 nm; *L*= 13-84 nm),[43] under conditions that would otherwise yield spherical NCs. This has been tentatively ascribed to *in-situ* generated $[Sn_xS_y]$ species (*e.g.*, $[Sn_2S_6]^{4-}$),[27,43] but the results presented above unambiguously demonstrate that the effect is actually due to the halides and that Sn(IV) is important only to the extent that it ensures the availability of sufficiently high halide concentrations in the growth solution. It is also clear that the formation of ultrathin $Cu_{2-x}S$ NSs results from a synergistic interaction between halides and Cu-alkanethiolate complexes that are formed *in-situ*, since the use of sulfur sources other than alkanethiols does not yield nanosheets (see above and Supporting Information, Figure S7).

Copper-thiolates have been extensively used as single source precursors to produce $Cu_{2-x}S$ NCs, both by solventless and solution based routes.[36,40,42-46] These synthetic protocols have yielded a wealth of different nanocrystal morphologies (*quasi*-spheres, hexagonal bipyramids and bifrustums, hexagonal nanodisks and nanoplatelets),[36,40,42-46] but ultrathin nanosheets are rare, and have been observed only when halides were present in the reaction medium (*e.g.*, ref. [27] and present work). The reaction mechanisms are not yet well-understood, although a recent *in-situ* synchrotron powder X-ray diffraction study has demonstrated that the C-S bond cleavage

is the limiting step in the formation and growth of colloidal $Cu_{2-x}S$ NCs by thermolysis of [Cu(DDT)] in solution.[44] Cu-alkanethiolates form a metal-organic framework (MOF) that is stable as a lamellar solid up to 143.5°C (for Cu-DDT), when it undergoes a phase transition to a mesogenic liquid crystal.[47] The structure of this liquid crystal phase is particularly relevant for the present discussion, as it consists of a hierarchically self-assembled hexagonal columnar mesophase, in which each column is made of a stack of tetranuclear $[Cu_4(DDT)_4]$ disks that are kept together by weaker Cu-S inter-disk interactions (Supporting Information, Figure S12). The irregularly shaped sheets observed at early reaction stages in this and other works[36,42] can thus be tentatively ascribed to intact Cu-thiolate frameworks. However, the inter-column and inter-disk interactions break at sufficiently high temperatures (*e.g.*, 205.6 °C for neat Cu-DDT) leading to an isotropic liquid (Supporting Information, Figure S12),[47] which, upon further heating, will undergo Cu-catalysed C-S thermolysis, producing independent $[Cu_4S_4]$ nuclei that further grow into *quasi*-spherical NCs or hexagonal nanodisks by monomer addition.[36,42] The different fate of the irregular sheets in the present work suggests that halides have a stabilizing effect on the Cu-thiolate framework, preserving its 2D-structural integrity at temperatures that are sufficiently high to sustain C-S thermolysis. Interestingly, recent work by Tao and co-workers has demonstrated that the ordered liquid crystalline mesophase plays an essential role in templating the nanocrystal morphology obtained by solventless thermolysis of Cu-thiolates, so that hexagonal $Cu_{2-x}S$ nanodisks and nanoplatelets are only obtained for Cu-thiolates that adopt an inverse columnar mesophase at the reaction temperature.[45] It is thus likely that the 2D-constrained growth observed in the present work is due to a templating framework formed by halides and the Cu-thiolate MOF.

Our experiments show that halides have a dramatic impact on both the optical spectra and the morphology of the Cu-thiolate precursor complexes formed upon heating of a mixture of Cu(I) salts and 1-DDT in ODE to 190 °C (Supporting Information, Figure S13). This temperature is just below the onset of C-S thermolysis, and therefore also below the nucleation threshold. The results presented in Fig. S13 thus reflect the properties of the precursor complexes formed in the reaction mixture. The presence of Br clearly affects the morphology of the Cu-thiolate precursor complex at room temperature, converting it from a 3D gel network (Supporting Information, Figure S13a) to irregularly shaped thin sheets (Supporting Information, Figure S13b). A 3D Cu-DDT gel has been observed before by Han and coworkers,[42] by cooling a solution of Cu-DDT in DDT from 200 °C to room temperature. It is interesting to note that this implies that the Cu-thiolate lamellar structure does not form under these conditions, suggesting that the inter-column Van der Waals interactions are weakened by the presence of the solvent molecules (ODE or DDT). The inter-disk Cu-S interactions are however sufficiently strong to keep the columns intact, allowing the formation of a 3D gel network of interconnected strings. The observation of 2D sheets in the presence of Br (Supporting Information, Figure S13b) can thus be interpreted as evidence that the inter-column interaction is reinforced by halides, allowing the formation of lamellar frameworks.

Halides may be expected to have a large impact on MOFs based on Cu(I) as connectors, since they are capable of binding as poly-coordinated bridging atoms between multiple (up to 4) Cu(I) atoms, often forming [(CuX)L]n (L= sulfur-donor ligand) coordination polymers with highly variable structures, ranging from 1D to 3D.[49] As will be discussed below, the pronounced changes observed in the optical spectra of the precursor complexes in the presence of halides (Figure 6, and Supporting Information, Figures S13d and S14) clearly demonstrate the formation

of direct bonds between halides and Cu(I) atoms in the Cu-thiolate complexes. The differences between the morphology of the $Cu_{2-x}S$ NCs obtained in the presence of Chloride and Bromide (ultrathin nanosheets, Figures 1-4) and Iodide (porous network of interconnected particles, Supporting Information Figure S11) suggests that the resulting Halide-Cu-thiolate MOFs have different geometries (2D for Cl and Br, 3D for I). This can be rationalized in terms of the different strengths of the Cu-X (X= Cl, Br, I) interactions, which are the strongest for Cu-I, rendering the geometry of (CuI)L coordination polymers dramatically different from those of (CuBr)L and (CuCl)L.[49]

Optical spectroscopy is thus particularly useful to unravel the role of the halides, since it allows the formation of $Cu_{2-x}S$ NCs to be followed, while simultaneously signaling the presence of precursors and intermediate reaction compounds. The optical spectra of samples collected during the synthesis (Figure 6, and Supporting Information, Figure S14) clearly show that halides have no effect on the identity of the complexes present prior to DDT injection, but dramatically affect the electronic structure of the Cu-thiolate complex formed immediately after the injection (Figure 6c). When no halides are added, an absorption transition is observed at 325 nm (Figure 6a), while in the presence of Br this absorption transition shifts to 375 nm (Figure 6b). We note that these spectra are identical to those obtained by heating up the reaction mixture to 190 °C (Supporting Information, Figure S13d) indicating that the same precursor complexes are formed. The photoluminescence (PL) of the Cu-thiolate precursor complexes also changes dramatically upon addition of halides (Figure 6a,b and Supporting Information, Figure S14). It is evident that these precursor complexes are consumed as the reaction progresses, since both the absorption and PL peaks associated with them decrease, while the characteristic absorption of

$Cu_{2-x}S$ increases (Figure 6a,b). This is consistent with the TEM observations discussed above (Figure 5).

The optical properties of the precursor complexes formed upon DDT injection are typical of polynuclear Cu(I) complexes with halides and sulfur-donor ligands.[48,49] Multinuclear Cu(I) complexes with sulfur or halide donors typically show efficient PL at room temperature, peaking at wavelengths ranging from 500 - 700 nm, depending on the ligands and the structure of the complex or coordination polymer.[48] The PL is often characterized by two independent bands, where the high energy PL peak originates from a Cu/halide-to-ligand charge transfer triplet state and the low energy PL peak originates from a $Cu_4X_4$ (X= donor atom, *i.e.* sulfur or halide) centered triplet state, which is a combination of X to Cu(I) charge-transfer and d-s transitions.[48] The low energy PL has larger Stokes shifts and longer lifetimes than the high energy PL. Moreover, the quantum yield of the high energy PL is lower, making it often absent at room temperature. The peak position, Stokes shift (*viz*., 1.3 eV) and lifetime (*viz*., 7.8 μs with a faster initial component of 1.8 μs, Supporting Information, Figure S14) observed for the Br-modified Cu-thiolate precursor complex are consistent with emission from the low energy state (*i.e*., the $Cu_4X_4$ centered triplet state). The large shifts induced in both the absorption and PL spectra by the presence of Br (*viz*., 0.34 eV and 0.48 eV, respectively) and the increase in the Stokes shift (from 1.17 to 1.3 eV) thus provide compelling evidence that Br atoms coordinate directly to Cu(I) atoms in the Cu-DDT precursor complexes. This is further supported by the dramatic increase observed in the PL QY in the presence of Br, since shorter Cu-Cu distances are known to lead to more efficient PL at RT.[48] It should be noted that the optical spectra provide no signatures of MSCs or stepwise growth,[50,51] thereby excluding mechanisms involving MSCs.

We propose that in the present case binding between halides (Br or Cl) and Cu(I) atoms in the Cu-thiolate precursor complexes leads to the formation of a soft 2D template that remains structurally intact beyond the onset of the C-S bond thermolysis. The thermally induced C-S bond cleavage is catalysed by the Cu(I) atoms,[52] and therefore only DDT molecules directly involved in the Cu-thiolate framework will undergo thermolysis. Since the C-S bond cleavage is the limiting step in the formation of colloidal $Cu_{2-x}S$ NCs by thermolysis of [Cu(DDT)] in solution,[44] the soft template will impose 2D constraints on the nucleation and growth of the $Cu_{2-x}S$ NCs, thereby leading to the formation of ultrathin colloidal $Cu_{2-x}S$ nanosheets. This mechanism is analogous to the nucleation and growth of colloidal NCs in solution,[53] except for the fact that it is two-dimensionally constrained. The impact of TOPO and of the overall concentration of the reaction system on the lateral dimensions and shape of the NSs can easily be understood from this perspective, since coordinating ligands are well-known to modulate the growth rates of colloidal NCs by competing with the monomers (*i.e.*, [CuS] units) for the binding sites, in a strongly facet-dependent fashion.[53] It is thus likely that both the final shape and the crystal structure of the NSs are determined by the interplay between the constraints imposed by the 2D soft template, the C-S thermolysis rates, and coordination by TOPO, halides and intact DDT molecules. It is interesting to note that the mechanism unraveled in the present work may be applicable also to the preparation of ultrathin 2D nanocrystals of other compositions, since lamellar metal thiolate complexes are widely used as single source precursors in the synthesis of nanocrystals of a variety of transition metal sulfides (*e.g.*, FeS, $Ni_3S_4$, $Cu_{2-x}S$, $Co_9S_8$, CdS, ZnS, PdS, $Ag_2S$, PbS and $Bi_2S_3$).[54-60] In this context, it is worth noting that recent work has demonstrated that $Ni_9S_8$ can exhibit 2D-growth, yielding colloidal nanocrosses, when nickel thiolate is used as single source precursor, provided halide ions are present in the reaction

medium.[61] In the absence of halides, only short nanorods are obtained. Although the authors of ref. [61] suggest a different mechanism to account for these observations (*viz*., halides would reduce the formation rate of nickel thiolate, thereby inhibiting nucleation and slowing down the growth kinetics, and, as a result, promoting 2D growth),[61] we argue that templating by a 2D halide-Ni-thiolate MOF is also a plausible mechanism.

**Composition tailoring by cation exchange.** Nanoscale cation exchange (CE) provides a versatile strategy for synthesizing colloidal NCs with compositions and morphologies that are not accessible by conventional methods.[34,35,51,62-68] Very often the anionic sublattice is not affected by the cation exchange, leading to a topotactic reaction, through which the size and shape of the parent NCs are preserved in the product NCs, despite the compositional change.[34,62] Interestingly, the degree of cation exchange can be controlled, leading to partial or total replacement of the native cation.[34,62] In the case of partial exchange, the elemental profile distribution within the product NC can also be controlled, so that core/shell heteronanocrystals,[65,66] homogeneous or gradient alloy nanocrystals,[66] and doped nanocrystals[67,68] can be obtained, depending on the chemical system and reaction conditions.[34,62,65-67] Topotactic CE reactions in which $Cu^+$ is exchanged for other cations have been extensively investigated in copper chalcogenides, yielding NCs with metastable shapes and structures that would otherwise not be attainable.[34,35,62-64]

In the present work, CE reactions were exploited to convert $Cu_{2-x}S$ NSs into CdS and ZnS NSs (Figure 7). The results show that the $Cu^+$ for $Cd^{2+}$ or $Zn^{2+}$ exchange reactions in $Cu_{2-x}S$ NSs are topotactic, thereby preserving the shape and size (both lateral dimensions and thickness) of the parent NSs in the product NSs. This is remarkable considering the ultrathin dimensions of the parent NSs, and implies that the sulfide anionic framework is very robust and can readily

accommodate and relax the local strain induced by the exchange of two $Cu^{+}$ ions by one $Cd^{2+}$ or $Zn^{2+}$ cation. This is in line with the crystal structure proposed for the $Cu_{2-x}S$ NSs (Figure 2e,f, and Supporting Information, Supporting discussion). The cation exchange did not reach completion, yielding Cu-doped CdS NSs and ZnS NSs. The doping level in the CdS NSs is sufficiently low to allow observation of efficient PL associated with exciton recombination in the $Cu^{+}$ dopants[69] (Supporting Information, Figure S15). These results demonstrate that the $Cu_{2-x}S$ NSs developed here can be used as well-defined morphological templates for the preparation of compositionally diverse NSs, thus allowing access to a whole range of novel ultrathin colloidal NSs that cannot be synthesized by direct routes.

## Conclusions

The novel "bottom-up" solution-based synthesis method developed in this work yields 2 nm thick colloidal $Cu_{2-x}S$ NSs with well-defined size and shape (hexagonal or triangular). The lateral dimensions of these ultrathin NSs can be tuned from 100 nm to 3 μm. These NSs are very robust and do not easily fold or aggregate, and therefore offer excellent solution processability. They can also be used as building blocks for self-organized superstructures. Moreover, we demonstrate that the composition of the NSs can be post-synthetically tailored by exploiting topotactic cation exchange reactions, while preserving their well-defined shape, lateral dimensions and thickness. The method presented here thus holds great promise as a route to solution-processable compositionally diverse ultrathin colloidal NSs with well-defined shape and size. It should be noted that combined control over surface, size, shape and composition can be used to modify the properties of the NSs or to bestow them with novel functionalities, paving the way towards tailor-made NSs.

***Supporting Information Available*:** Additional details on the characterization methods, discussion on the crystal structure of tetragonal $Cu_{2-x}S$, low-angle XRD patterns of two different samples of $Cu_{2-x}S$ nanosheets, elemental mapping of a selected nanosheet, Table summarizing the outcome of all the control syntheses, TEM images of samples prepared under various different conditions, optical data (absorption, PL, and PLE spectra, PL decay curves) of samples collected immediately after the injection of DDT into the reaction mixture, optical spectra (absorption, PL, PLE) of Cu-doped ultrathin CdS nanosheets. This material is available free of charge *via* the Internet at http://pubs.acs.org.

***ACKNOWLEDGMENTS***. W.v.d.S. and C.d.M.D. acknowledge financial support from the division of Chemical Sciences (CW) of the Netherlands Organization for Scientific Research (NWO) under grant number ECHO.712.012.001. The authors are grateful to Johannes D. Meeldijk (Utrecht University) for his assistance regarding TEM-EDS measurements. X.K. and S.B. acknowledge funding from the European Research Council under the Seventh Framework Program (FP7) ERC Grant No 246791 – COUNTATOMS and ERC Grant No335078-COLOURATOM. Financial support from the EU FP7-Integrated Infrastructure Initiative-I3 program ESTEEM2(312483) is gratefully acknowledged.

**REFERENCES**

1. Butler, S. Z.; Hollen, S. M.; Cao, L.; Cui, Y.; Gupta, J. A.; Gutie, H. R.; Heinz, T. F.; Hong, S. S.; Huang, J.; Ismach, A. F. *et al. ACS Nano* **2013**, *7*, 2898-2926.

2. Wang, Q. H.; Kalantar-Zadeh, K.; Kis, A.; Coleman, J. N.; Strano, M. S. *Nature Nanotechnol.* **2012**, *7*, 699-712.

3. Xu, M.; Liang, T.; Shi, M.; Chen, H. *Chem. Rev.* **2013**, *113*, 3766-3798.

4. Chhowalla, M.; Shin, H. S.; Eda, G.; Li, L.-J.; Loh, K. P.; Zhang, H. *Nature Chem.* **2013**, *5*, 263-275.

5. Rao, C. N. R.; Ramakrishna Matte, H. S. S.; Maitra, U. *Angew. Chem. Int. Ed.* **2013**, *52*, 13162-13185.

6. Rogers, J. A.; Lagally, M. G.; Nuzzo, R. G. *Nature* **2011**, *477*, 45-53.

7. Narita, A.; Feng, X.; Hernandez, Y.; Jensen, S. A.; Bonn, M.; Yang, H.; Verzhbitskiy, I. A.; Casiraghi, C.; Hansen, M. R.; Koch, A. H. R. *et al. Nature Chem.* **2014**, *6*, 126-132.

8. Yin, Z.; Zhu, J.; He, Q.; Cao, X.; Tan, C.; Chen, H.; Yan, Q.; Zhang, H. *Adv. Energy Mater.* **2014**, *4*, 1300574.

9. Huang, X.; Tan, C.; Yin, Z.; Zhang, H. *Adv. Mater*. **2014**, *26*, 2185-2204.

10. Bouet, C.; Tessier, M. D.; Ithurria, S.; Mahler, B.; Nadal, B.; Dubertret, B. *Chem. Mater.* **2013**, *25*, 1262-1271.

11. Ithurria, S.; Bousquet, G.; Dubertret, B. *J. Am. Chem. Soc.* **2011**, *133*, 3070-3077.

12. Li. Z.; Peng, X. *J. Am. Chem. Soc.* **2011**, *133*, 6578-6586.

13. Hutter, E. M.; Bladt, E.; Goris, B.; Pietra, F.; van der Bok, J. C.; Boneschanscher, M. P.; de Mello Donega, C.; Bals, S.; Vanmaekelbergh, D. *Nano Lett.* **2014**, *14* 6257-6262.

14. Yang, J.; Son, J. S.; Yu, J. H.; Joo, J.; Hyeon, T. *Chem. Mater.* **2013**, *25*, 1190-1198.

15. Son, J. S.; Park, K.; Kwon, S. G.; Yang, J.; Choi, M. K.; Kim, J.; Yu, J. H.; Joo, J.; Hyeon, T. *Small* **2012**, *8*, 2394-2402.

16. Yu, J. H.; Liu, X.; Kweon, K. E.; Joo, J.; Park, J.; Ko, K.-T.; Lee, D. W.; Shen, S.; Tivakornsasithorn, K.; Son, J. S. *et al. Nature Mater.* **2010**, *9*, 47-53.

17. Liu, Y. H.; Wang, F. D.; Wang, Y. Y.; Gibbons, P. C.; Buhro, W. E. *J. Am. Chem. Soc.* **2011**, *133*, 17005-17013.

18. Ithurria, S.; Tessier, M. D.; Mahler, B.; Lobo, R. P. S. M.; Dubertret, B.; Efros, A. L. *Nature Mater.* **2011**, *10*, 936-941.

19. Pelton, M.; Ithurria, S.; Schaller, R. D.; Dolzhnikov, D. S.; Talapin, D. V. *Nano Lett.* **2012**, *12*, 6158-6163.

20. Tessier, M. D.; Mahler, B.; Nadal, B.; Heuclin, H.; Pedetti, S.; Dubertret, B. *Nano Lett.* **2013**, *13*, 3321-3328.

21. Malakooti, R.; Cademartiri, L.; Migliori, A.; Ozin, G. A. *J. Mater. Chem.* **2008**, *18*, 66–69.

22. Li, L.; Chen, Z.; Hu, Y.; Wang, X.; Zhang, T.; Chen, W.; Wang, Q. *J. Am. Chem. Soc.* **2013**, *135*, 1213-1216.

23. Schliehe, C.; Juarez, B. H.; Pelletier, M.; Jander, S.; Greshnykh, D.; Nagel, M.; Meyer, A.; Foerster, S.; Kornowski, A.; Klinke, C. *et al. Science* **2010**, *329*, 550-553.

24. Morrison, P. J.; Loomis, R. A.; Buhro, W. E. *Chem. Mater.* **2014**, *26*, 5012–5019.

25. Park, H.; Chung, H.; Kim, W. *Mater. Lett.* **2013**, *99*, 172-175.

26. Park, K. H.; Jang, K.; Son, S. U. *Angew. Chem. Int. Ed.* **2006**, *45*, 4608-4612.

27. Yi, L.; Gao, M. *Cryst. Growth Des.* **2011**, *11*, 1109-1116.

28. Zhao, Y.; Burda, C. *Energy Environ. Sci.* **2012**, *5*, 5564-5576.

29. Wadia, C.; Alivisatos, A. P.; Kammen, D. M. *Environ. Sci. Technol.* **2009**, *43*, 2072-2077.

30. Luther, J. M.; Jain, P. K.; Ewers, T.; Alivisatos, A. P. *Nature Mater.* **2011**, *10*, 361-366.

31. Kriegel, I.; Jiang, C.; Rodríguez-Fernández, J.; Schaller, R. D.; Talapin, D. V.; da Como, E.; Feldmann, J. *J. Am. Chem.Soc.* **2012**, *134*, 1583-1590.

32. Hsu, S. W.; Ngo, C.; Tao, A. R. *Nano Lett.*, **2014**, *14*, 2372-2380.

33. Goel, S.; Chen, F.; Cai, W. *Small* **2014**, *10*, 631-645.

34. Beberwyck, B. J.; Surendranath, Y.; Alivisatos, A. P. *J. Phys. Chem. C* **2013**, *117*, 19759- 19770.

35. Li, H.; Brescia, R.; Povia, M.; Prato, M.; Bertoni, G.; Manna, L.; Moreels, I. *J. Am. Chem. Soc.* **2013**, *135*, 12270-12278.

36. Wang, Y.; Hu, Y.; Zhang, Q.; Ge, J.; Lu, Z.; Hou, Y.; Yin, Y. *Inorg. Chem.* **2010**, *49*, 6601–6608.

37. Son, D. H.; Hughes, S. M.; Yin, Y.; Alivisatos, A. P. *Science* **2004**, *306*, 1009–1012.

38. Pileni, M. P. *J. Phys. Chem. B* **2001**, *105*, 3358-3371.

39. Chakrabarti, D.J.; Laughlin, D.E. *Bull. Alloy Phase Diagrams* **1983**, *4*, 254-270.

40. Li, W.; Shavel, A.; Guzman, R.; Rubio-Garcia, J.; Flox, C.; Fan, J.; Cadavid, D.; Ibáñez, M.; Arbiol, J.; Morante, J. R.; Cabot, A. *Chem. Commun.* **2011**, *47*, 10332-10337.

41. Du, Y.; Yin, Z.; Zhu, J.; Huang, X.; Wu, X.-J.; Zeng, Z.; Yan. Q.; Zhang, H. *Nature Commun.*, **2012**, *3*, 1177.

42. Han, W.; Yi, L.; Zhao, N.; Tang, A.; Gao, M.; Tang, Z. *J. Am. Chem. Soc.* **2008**, *130*, 13152-13161.

43. Li, X.; Shen, H.; Niu, J.; Li, S.; Zhang, Y.; Wang, H.; Li, L. S. *J. Am. Chem. Soc.* **2010**, *132*, 12778-12779.

44. Noerby, P.; Johnsen, S.; Iversen, B. B. *ACS Nano* **2014**, *8*, 4295-4303.

45. Bryks, W.; Wette, M.; Velez, N.; Hsu, S.-W.; Tao, A. R. *J. Am. Chem. Soc.* **2014**, *136*, 6175–6178.

46. Sigman, M. B.; Ghezelbash, A.; Hanrath, T.; Saunders, A. E.; Lee, F.; Korgel, B. A. *J. Am. Chem. Soc.*, **2003**, *125*, 16050-16057.

47. Espinet, P.; Lequerica, M. C.; Martın-Alvarez, J. M. *Chem. Eur. J.* **1999**, *5*, 1982-1986.

48. Ford, P. C.; Cariati, E.; Bourassa, J. *Chem. Rev.* **1999**, *99*, 3625-3648.

49. Lapprand, A.; Bonnot, A.; Knorr, M.; Rousselin, Y.; Kubicki, M. M.; Fortin, D.; Harvey, P. D. *Chem. Commun.* **2013**, *49*, 8848–8850.

50. Groeneveld, E.; van Berkum, S.; Meijerink, A.; Donega, C. d. M. *Small* **2011**, *7*, 1247-1256.

51. Groeneveld, E.; van Berkum, S.; van Schooneveld, M. M.; Gloter, A.; Meeldijk, J. D.; van den Heuvel, D. J.; Gerritsen, H. C.; Donega, C. d. M. *Nano Letters* **2012**, *12*, 749-757.

52. Wang, L.; He, W.; Yu, Z. *Chem. Soc. Rev.* **2013**, *42*, 599-621.

53. Donega, C. d. M. *Chem. Soc. Rev.* **2011**, *40*, 1512-1546.

54. Zhuang, Z.; Lu, X.; Peng, Q.; Li, Y. *Chem. Eur. J.* **2011**, *17*, 10445–10452.

55. Tang, A.; Wang, Y.; Ye, H.; Zhou, C.; Yang, C.; Li, X.; Peng, H.; Zhang, F.; Hou, Y.; Teng, F. *Nanotechnology* **2013**, *24*, 355602.

56. Wang, Y.; Tang, A.; Li, K.; Yang, C.; Wang, M.; Ye, H.; Hou, Y.; Teng, F. *Langmuir* **2012**, *28*, 16436-16443.

57. Busupalli, B.; Kummara, S.; Kumaraswamy, G.; Prasad, B. L. V. *Chem. Mater*. **2014**, *26*, 3436-3442.

58. Shi, W.; Zhu, J.; Rui, X.; Cao, X.; Chen, C.; Zhang, H.; Hng, H. H.; Yan, Q. *ACS Appl. Mater. Interfaces* **2012**, *4*, 2999-3006.

59. Chen, J.; Wu, L. M.; Chen, L. *Inorg. Chem.* **2007**, *46*, 586-591.

60. Xu, C.; Zeng, Y.; Rui, X.; Xiao, N.; Zhu, J.; Zhang, W.; Chen, J.; Liu, W.; Tan, H.; Hng, H. H.; *et. al*. *ACS Nano* **2012**, *6*, 4713-4721.

61. Wu, W.Y; Chakraborty, S.; Chang, C. K. L.; Guchhait, A.; Lin, M.; Chan, Y. *Chem. Mater*. **2014**, *26*, 6120-6126.

62. Rivest, J. B.; Jain P. K. *Chem. Soc. Rev.* **2013**, *42*, 89-96.

63. Li, H.; Zanella, M.; Genovese, A.; Povia, M.; Falqui, A.; Giannini, C.; Manna, L. *Nano Lett.* **2011**, *11*, 4964-4970.

64. van der Stam, W.; Gantapara, A. P.; Akkerman, Q. A.; Soligno, G.; Meeldijk, J. D.; van Roij, R.; Dijkstra, M.; Donega, C. d. M. *Nano Lett.* **2014**, *14*, 1032-1037.

65. Casavola, M.; van Huis, M. A.; Bals, S.; Lambert, K.; Hens, Z.; Vanmaekelbergh, D. *Chem. Mater.* **2012**, *24*, 294-302.

66. Groeneveld, E.; Witteman, L.; Lefferts, M.; Ke, X.; Bals, S.; van Tendeloo, G.; Donega, C. d. M. *ACS Nano* **2013**, *7*, 7913-7930.

67. Eilers, J.; Groeneveld, E.; Donega, C. d. M.; Meijerink, A. *J. Phys. Chem. Lett.* **2012**, *3*, 1663-1667.

68. Sahu, A.; Kang, M. S.; Kompch, A.; Notthoff, C.; Wills, A. W.; Deng, D.; Winterer, M.; Frisbie, C. D.; Norris, D. J. *Nano Lett.* **2012**, *12*, 2587–2594.

69. Tang, A.; Yi, L.; Han, W.; Teng, F.; Wang, Y.; Hou, Y.; Gao, M. *Appl. Phys. Lett.* **2010**, *97*, 033112.

## FIGURES

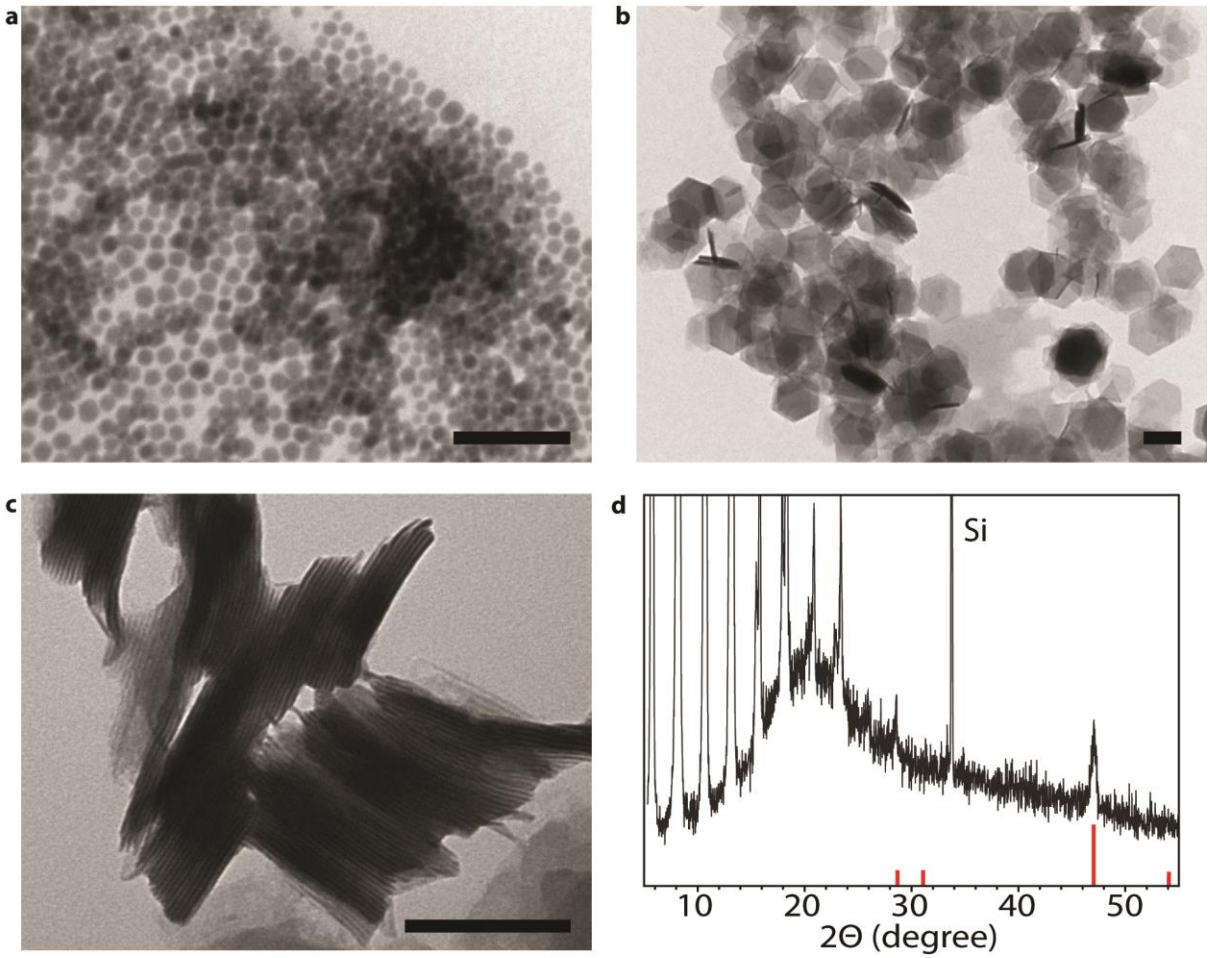


**Figure 1.** Transmission Electron Microscopy (TEM) images of colloidal $Cu_{2-x}S$ nanocrystals synthesized in the absence (**a**) and in the presence (**b,c**) of $SnBr_4$, under otherwise identical conditions. Scale bars correspond to 100 nm. (**d**) XRD pattern of a sample of $Cu_{2-x}S$ nanosheets similar to those shown in (**b,c**), which was deposited from a toluene solution on a silicon substrate (see also Supporting Information, Figure S1). The XRD pattern of digenite (JCPDS card no. [47-1748]) is shown as reference (red lines).

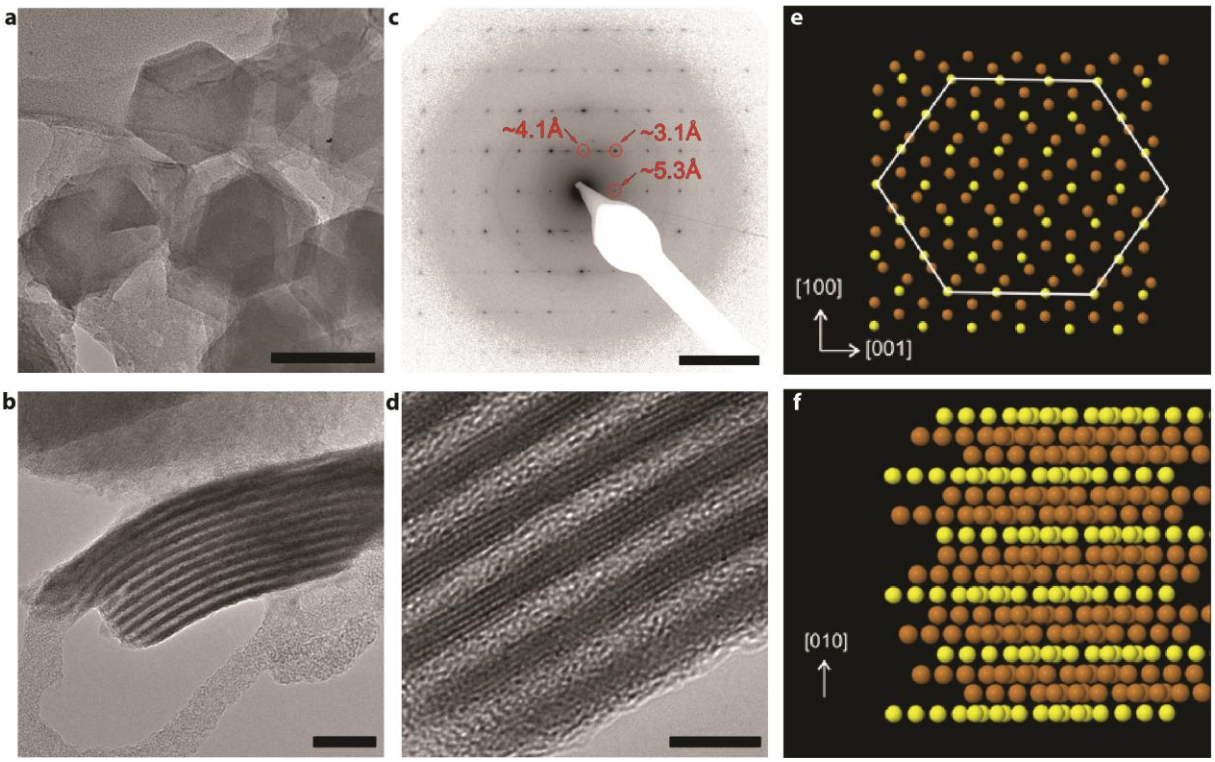


**Figure 2.** TEM characterization of ultrathin colloidal $Cu_{2-x}S$ nanosheets (NSs). (**a**) Overview of NSs lying flat on the TEM grid (scale bar: 100 nm). (**b**) Side view of a NS stack, highlighting the uniformity of both the NS thickness and the inter-NS separation (scale bar: 20 nm). (**c**) Diffraction pattern (DP) taken from a single NS (scale bar: 5.0 $nm^{-1}$). (**d**) High-resolution TEM image (scale bar: 5 nm), showing a detail of the stack presented in (**b**). The crystallinity of the NSs is clearly observed in this projection. **e,f)** Atomic model of the tetragonal $Cu_2S$ structure. The brown and yellow spheres depict Cu and S atoms, respectively (see also Supporting Information, Supporting Discussion). **e)** Projection along the *b*-axis of the tetragonal structure. The tetragonal *a* and *c* axes are indicated. It now becomes clear why the outer morphology of the NSs can be hexagonal, whereas the crystal structure is tetragonal. **f**) Perspective view of the atomic structure with the *b* axis pointing upward. The buckled Cu layers are visible, corresponding to the atomic layers with dark contrast in the HRTEM image shown in (d).

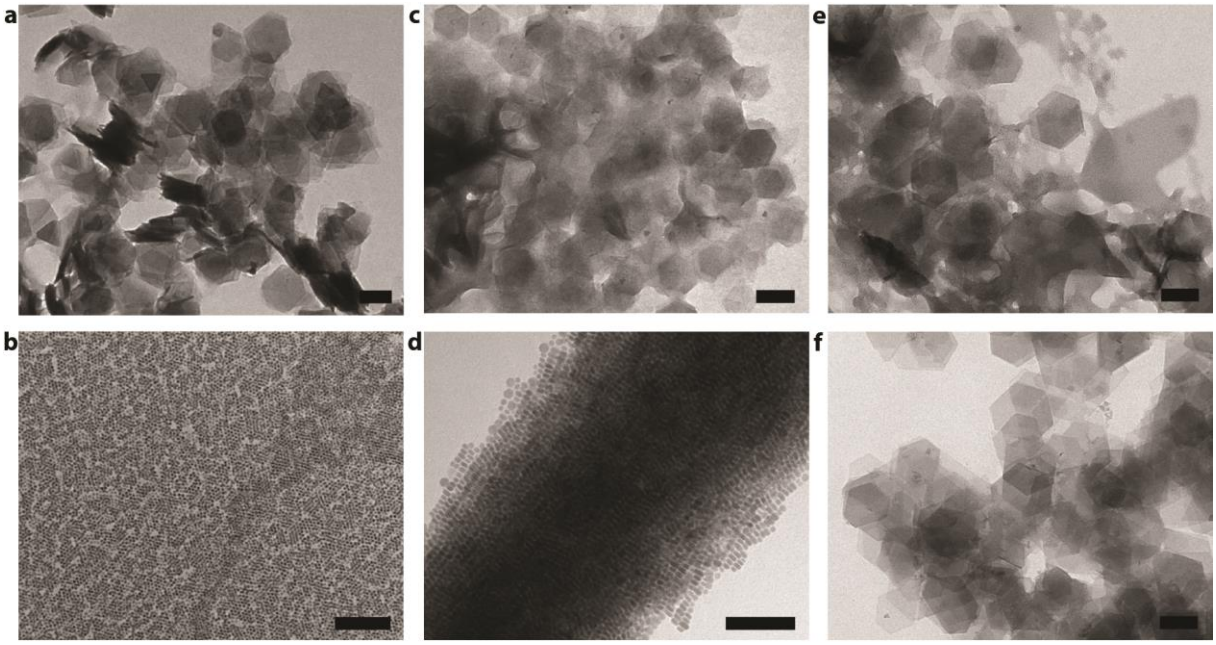


**Figure 3.** TEM images of colloidal $Cu_{2-x}S$ NCs obtained with different additives. The composition of the reaction medium and reaction conditions are identical in all cases, except for the additive. Scale bars correspond to 100 nm. (**a**) $SnBr_4$. (**b**) $Sn(acetate)_4$. (**c**) $SnBr_4$, but its concentration is 1/2 of that used in (a). (**d**) $SnBr_4$, but its concentration is 1/4 of that used in (a). (**e**) No additive, but Cu(acetate) is replaced by CuBr. (**f**) NaBr as additive and CuBr instead of Cu(acetate).

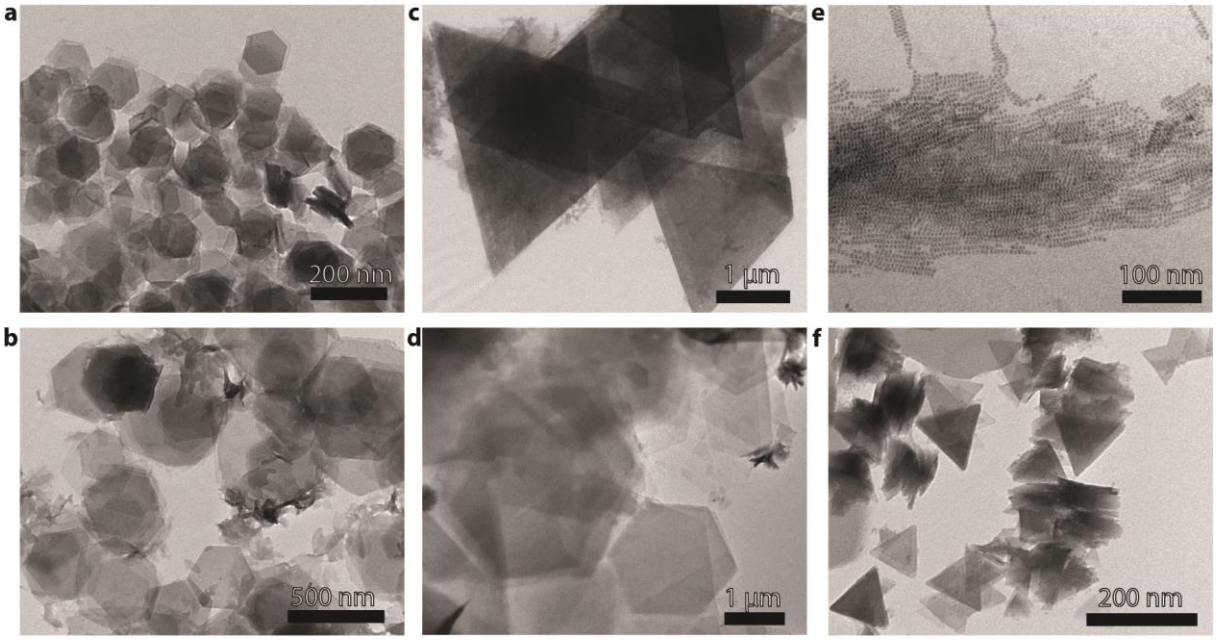


**Figure 4.** TEM images of colloidal $Cu_{2-x}S$ NCs obtained under different reaction conditions. (**a**) 17 mM Cu(acetate), 5.8 mM $SnBr_4$ and 0.1 M TOPO in ODE; injection of 2.1 mmol DDT. (**b**) Same as (**a**), but diluted by a factor 4 with ODE. (**c**) Same as (**a**) but without TOPO. (**d**) Same as (**a**) but TOPO concentration reduced to 20 mM. (**e**) $SnCl_4$ instead of $SnBr_4$, while keeping all concentrations unchanged. (**f**) $SnCl_4$ instead of $SnBr_4$, but $SnCl_4$ concentration increased by a factor 3.

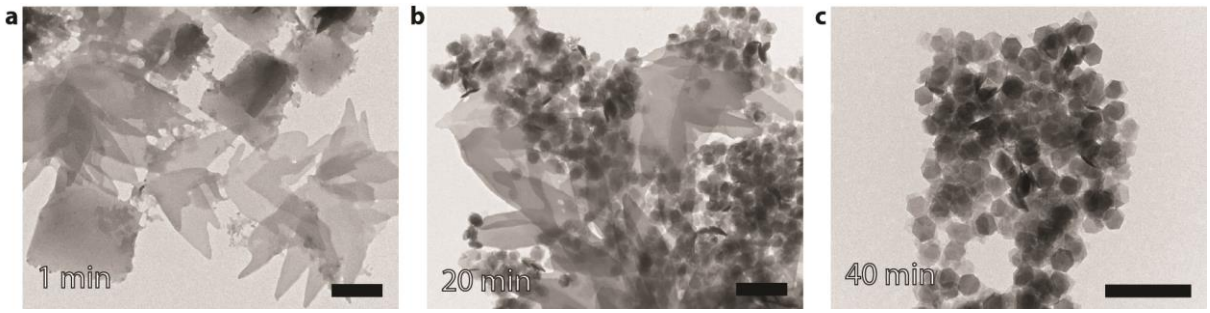


**Figure 5.** TEM images of samples collected at different time points after the injection of DDT into a solution of Cu(I) acetate, $SnBr_4$ and TOPO in ODE at 220 °C (scale bars correspond to 500 nm).

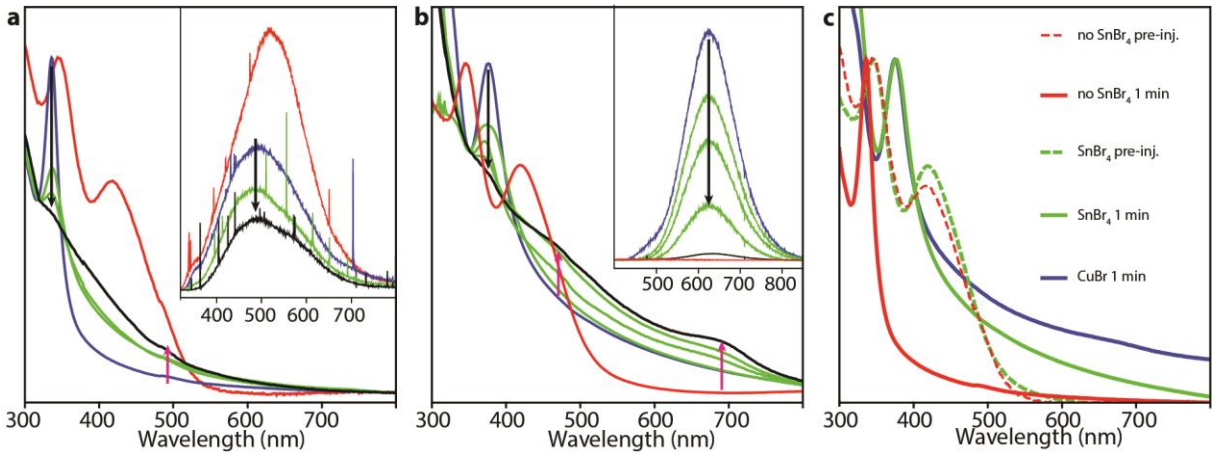


**Figure 6.** (**a**,**b**) Temporal evolution of the absorption and PL (insets) spectra of samples collected at different time points during $Cu_{2-x}S$ NC syntheses performed without (**a**) and with $SnBr_4$ (**b**). The reaction conditions and composition of the reaction mixture were identical in both cases, except for the presence or absence of $SnBr_4$. Red and blue lines give, respectively, the spectra prior to and 1 min after DDT injection. Black lines correspond to the final samples, collected at 15 min for (**a**) (9 nm $Cu_{2-x}S$ NCs), and 80 min for (**b**) (ultrathin hexagonal $Cu_{2-x}S$ NSs). Intermediate time points are given by green lines (4, 10 min in **a**; 4, 15, 33 min in **b**). The PL excitation spectrum and PL decay curve of the Br-modified Cu-thiolate precursor complex are shown in Supporting Figure S14. The arrows indicate the evolution of the peak intensities, and show that Cu-thiolate (black arrow) is consumed as $Cu_{2-x}S$ (purple arrow) forms. (**c**) Comparison of the absorption of samples collected prior to and 1 min after injection.

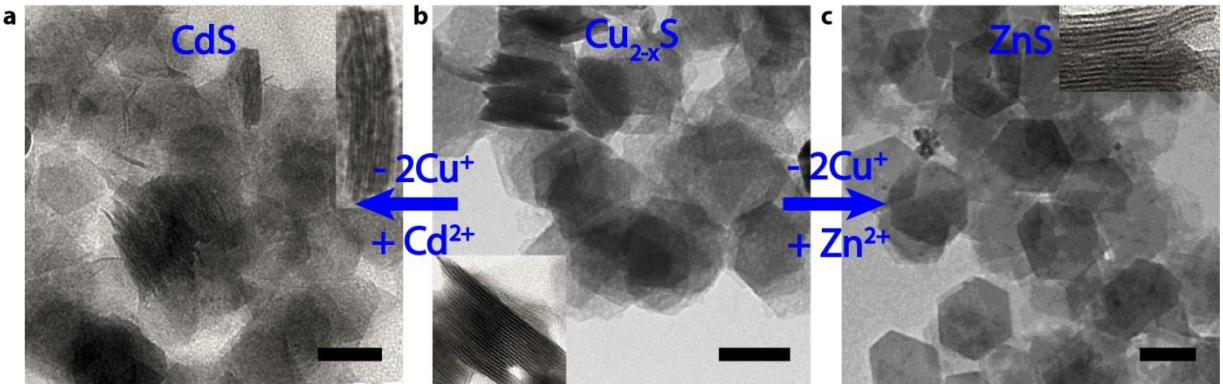


**Figure 7.** TEM images of ultrathin colloidal nanosheets (NSs) of various compositions (insets show stacks of NSs): (**a**) NSs obtained after $Cu^{+}$ for $Cd^{2+}$ exchange in $Cu_{2-x}S$ NSs (ratio Cd: S: Cu: Br= 0.90±0.04: 1.0: 0.06±0.01: 0.03±0.01) (**b**) $Cu_{2-x}S$ NSs used as parent NCs for the NSs shown in **a** and **c** (ratio S: Cu: Br= 1.0: 2.0±0.2: 0.30±0.06); (**c**) NSs obtained after $Cu^{+}$ for $Zn^{2+}$ exchange in $Cu_{2-x}S$ NSs (ratio Zn: S: Cu: Br= 0.97±0.04: 1.0: 0.30±0.06: 0.10±0.02).

*Chemistry of Materials* **2015**, *27*, **283-291. DOI: 10.1021/cm503929q**

## Table of Contents graph